An Improved Non-Isolated Resonant Converter With Integrated Magnetics for Data Center Applications

Zewei LI, Yuanchi ZHANG, Yu ZHANG, Yujie CHENG, Yan XING, and Hongfei WU

***Abstract*—An improved non-isolated resonant converter with integrated magnetics is proposed to achieve high step-down voltage conversion ratio for 48 V data center applications. The non-isolated resonant converter is composed of autotransformer cell and LLC resonant cell. The outputs of the two cells are in parallel to achieve higher output current. By adopting a symmetrical half-bridge circuit structure, the risk of DC bias in high-frequency transformers is addressed, and balanced current stress on synchronous rectifier switches is achieved. Magnetic integration of the autotransformer and high frequency transformer is proposed to achieve higher power density and higher efficiency. Topology, operation principle, integrated magnetic design and implementation of the proposed non-isolated resonant converter are analyzed in detail. Experimental prototype with 8:1 conversion ratio is developed for the front-end bus converter of 48 V data-center power systems. The power density of the prototype is 1.734 kW/in^3, and the maximum efficiency is 98.2%.**

***Index Terms*—Bus converter, data center, magnetic integration, non-isolated, resonant converter.**

I. Introduction

WITH the development of emerging information technologies such as 5G communication, big data computing, and cloud computing, the number of data centers grows rapidly. The energy consumption of data centers also grows sharply. By 2030, the electricity consumption of data centers will account for 8% of the world's total electricity consumption [1]. The huge energy consumption has become a constraint factor for the large-scale development of data centers.

The architecture of power supply system directly affects the energy efficiency. As shown in Fig. 1(a), the traditional 12 V power supply architecture has been unable to adapt to the development of the new generation of data center technology due to problems such as multi-stage power conversion, high power distribution network losses, etc. The 48 V power supply architecture shown in Fig. 1 (b) can reduce the power conversion stages. It significantly reduces line loss and is more suitable for high-capacity data centers. According to [2], the efficiency of 48 V power supply architecture is 6% higher than the traditional 12 V architecture. However, how to achieve a high step-down ratio, high efficiency, and high-power density power conversion between the 48 V DC bus and sub-1V load has become a new challenge for the 48 V data center power supply system [3].

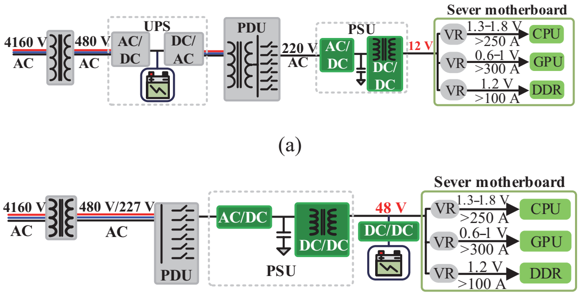

(a)

(b)

Fig. 1. Power supply system architecture. (a) 12 V architecture and (b) 48 V architecture.

For 48 V power supply systems, two-stage and single-stage solutions are available. Because the low voltage and high current point of load (POL) converter has been mature, the two-stage solution composed of an intermediate bus converter and POL converters has been paid more attention [4]–[7]. To improve the efficiency of POL converter, it is required to reduce the intermediate bus voltage as much as possible. Therefore, the bus converters with high step-down ratio have become the main focus of the two-stage power supply [8], [9].

Switched-capacitor converters use only switches and capacitors for voltage conversion. Due to the high energy density of capacitors, it is easy to achieve high-density integration. Many circuit topologies, design and implementation technologies have been proposed for switched-capacitor converters [10]–[13]. However, as the voltage ratio of the switched capacitor converter increases, the number of switches increases exponentially, leading to a significant increase of conduction loss.

The transformer-based LLC resonant converter can improve the voltage conversion rate by increasing the transformer turn ratio. It has the characteristics of soft switching, which can easily realize high-power density integration of the converter. Meanwhile, matrix transformer, magnetic integration and other technologies can improve the power processing ability

---

Manuscript received May 7, 2024; revised June 19, 2024; accepted July 18, 2024. Date of publication September 30, 2024; date of current version August 30, 2024. This work was supported by the National Natural Science Foundation of China under Grants 52122708. *(Corresponding author: Hongfei Wu)*

All authors are with the College of Automation, Nanjing University of Aeronautics and Astronautics, Nanjing 210016, China (e-mail: lizewei@nuaa.edu.cn; ZhangYuanchi@nuaa.edu.cn; zhangyu1010@nuaa.edu.cn; zhaolumuzhu@163.com; xingyan@nuaa.edu.cn; wuhongfei@nuaa.edu.cn).

Digital Object Identifier 10.24295/CPSSTPEA.2024.00014

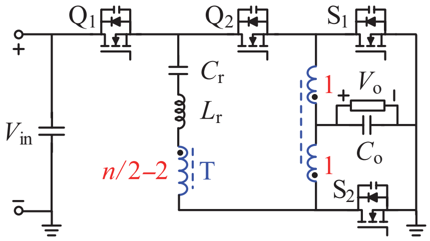

Fig. 2. Topology of the non-isolated resonant converter [16].

and power density [14], [15]. Therefore, the transformer-based LLC resonant converters have been widely concerned in high step-down ratio, low voltage and high current scenarios [6], [9]. However, due to the existence of the magnetic core and high current windings, the power density of the transformer-based LLC resonant converter is lower than the switched capacitor converters.

To achieve high efficiency and high-power density, non-isolated resonant converters is a good choice [16]–[19]. Compared with the traditional isolated resonant converter, part of the power in the non-isolated resonant converter is transferred directly from the input to the output. It can reduce the turn ratio and current stress of the transformer when achieve the same voltage conversion ratio.

In [16], a family of non-isolated resonant converters is proposed, among which the non-isolated half-bridge resonant converter shown in Fig. 2 has a simple structure and achieve high step-down ratio with reduced transformer turns ratio. In addition, the current through the secondary winding will be reduced due to the partial power conversion characteristic. So, the transformer loss is reduced. However, since all output current will pass through the secondary winding of the transformer. When the output current is higher, the winding loss of the transformer will be greater. Meanwhile, according to the current waveform provided in [16], the currents flowing through S_1 and S_2, i_{S1} and i_{S2} are different. If the on-impedance of S_1 and S_2 is the same, the voltage drop of the two switches will be different, leading to dc-bias issue of the transformer.

To achieve high conversion ratio, high efficiency and high-power density, this paper proposes an improved non-isolated half-bridge resonant converter based on the non-isolated resonant converter shown in Fig 2. It has a matrix output structure and is suitable for higher output current applications. In addition, the symmetrical structure of the proposed converter solves the dc-bias issue of transformer. This paper is organized as follows: Section II demonstrates the topology and operating principle of the proposed hybrid resonant converter. Section III presents the magnetic core integration design of hybrid resonant converter. Section IV shows the experimental results. At last, Section V concludes the paper.

II. Topology and Operation Principle

A. Topology of Improved Non-Isolated Resonant Converter

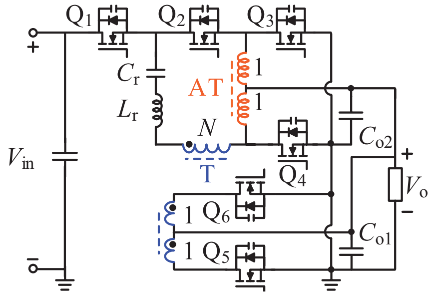

Fig. 3. Topology of a novel non-isolated resonant converter.

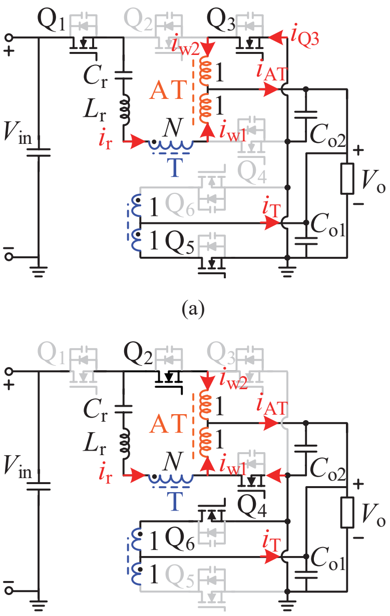

(a)

(b)

Fig. 4. The equivalent circuit of the two main switching modes. (a) Mode I and (b) Mode II.

Based on the non-isolated resonant converter shown in Fig. 2, a new novel non-isolated resonant converter is evolved. The coupled primary and secondary windings of the transformer in Fig. 2 can be separated. The separated secondary windings work as an autotransformer. Then, the new secondary windings and the rectification unit are configured for the primary side. Thus, as shown in Fig. 3, a novel non-isolated resonant converter is proposed, where a 2:1 autotransformer AT and a transformer T are employed. The resonant inductor L_r, resonant capacitor C_r and transformer T constitute an LLC resonant circuit. It indicates that the operation of the novel non-isolated resonant converter is quite similar to the well-known LLC resonant converter. Soft-switching of all the switches can be achieved easily.

In contrast to the non-isolated resonant converter shown in Fig. 2, the converter shown in Fig. 3 includes autotransformer cell and LLC resonant cell. The secondary-side outputs of both the two cells are in parallel, which can help to extend the output current capability and make the converter suitable for lower-voltage higher-current applications.

The two main operating modes of the novel non-isolated resonant converter are shown in Fig. 4. The switches Q_1, Q_3

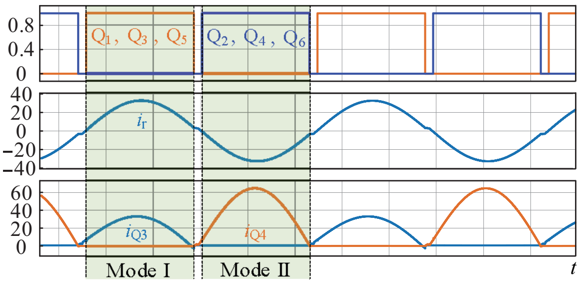

Fig. 5. Simulation waveform of a novel non-isolated resonant circuit ($N = 2$).

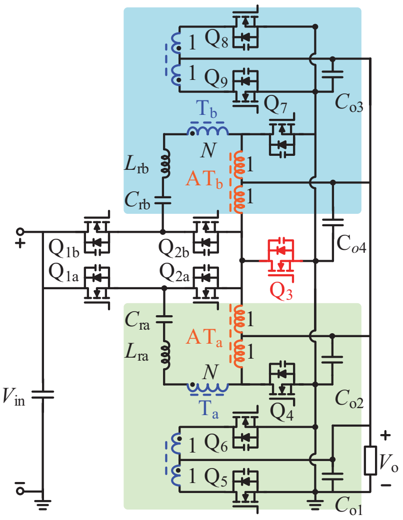

Fig. 6. Topology of two parallel non-isolated resonant converters with common switch.

and Q_5 are simultaneously conducting and are complementary to Q_2, Q_4 and Q_6.

When operating in Mode I, Q_1, Q_3 and Q_5 are on. The current i_{Q3} through Q_3 is equal to i_{w2} which is the autotransformer winding current. The autotransformer winding current i_{w1} is equal to the resonant current i_r. At the same time, the winding currents of the autotransformer, i_{w1} and i_{w2}, are equal because of the 1:1 winding turn ratio. So, there is $i_{Q3} = i_{w1} = i_{w2} = i_r$.

When operating in Mode II, the current i_{Q4} flowing through Q_4 is equal to $i_{w1}–i_r$. The i_{w1} and i_{w2} are also equal to the resonant currents $–i_r$. So, there is $i_{Q4} = i_{w1}–i_r = –2i_r$.

The current flowing through Q_4 is always twice that flowing through Q_3. Fig. 5 shows the simulation waveform with the turns ratio N of the transformer being 2, where i_{Q4} is twice i_{Q3}. The novel non-isolated resonant converter also has the dc-bias issue of the transformer.

To address the dc-bias issue of the transformer, the novel non-isolated resonant converter shown in Fig. 3 must be improved. In order to balance the current stress of switching tubes Q_3 and Q_4, two novel non-isolated resonant converters shown in Fig. 3 are connected in parallel, and the switches with less current stress are shared. A non-isolated resonant converter with a common switch Q_3, as shown in Fig. 6, is obtained. In this topology, the current stress of each autotransformer synchronous rectifier is consistent. Meanwhile, the switches Q_{1a} and Q_{1b}, Q_{2a} and Q_{2b} in Fig. 6 operate simultaneously, respectively. The Q_{1a} and Q_{1b} can be replaced by a switch Q_1, and Q_{2a} and Q_{2b} can be replaced by a switch Q_2, evolving to the improved non-isolated resonant converter, as shown in Fig.7. The converter also uses a common resonant capacitor C_r, to ensure that the parameters of the two resonators are consistent. The improved non-isolated resonant circuit is a symmetrical half-bridge circuit structure. It effectively solves the dc-bias issue of the transformer caused by the unequal current stress of each synchronous rectifier of autotransformer.

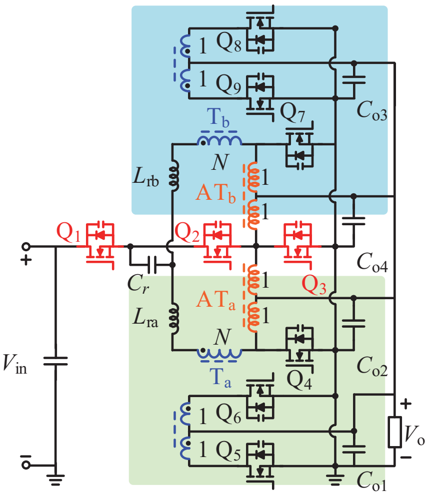

Fig. 7. Topology of the improved non-isolated resonant converter.

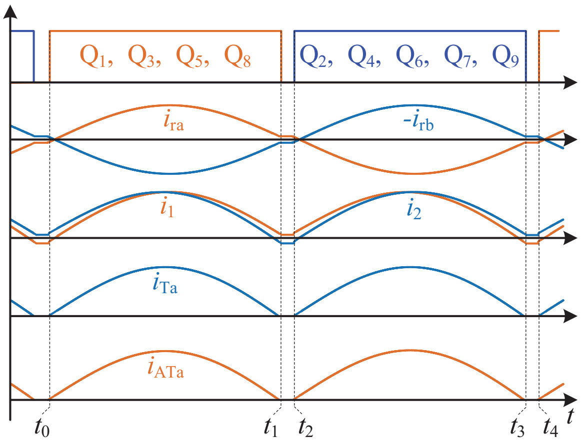

Fig. 8. Operating waveforms of the improved non-isolated resonant converter.

B. Operation Principles and Voltage Gain Characteristics

To make the improved non-isolated resonant converter work in an optimal operating state, the switching frequency f_s is equal to the resonant frequency f_r. The resonant frequency can be expressed as:

$$f_r = \frac{1}{2\pi \cdot \sqrt{L_{ra} \cdot C_r / 2}} = \frac{1}{2\pi \cdot \sqrt{L_{rb} \cdot C_r / 2}} \tag{1}$$

The main operating waveform of the improved non-isolated resonant converter is shown in Fig. 8, where $f_s = f_r$. There are four switching modes in a switching cycle, the equivalent

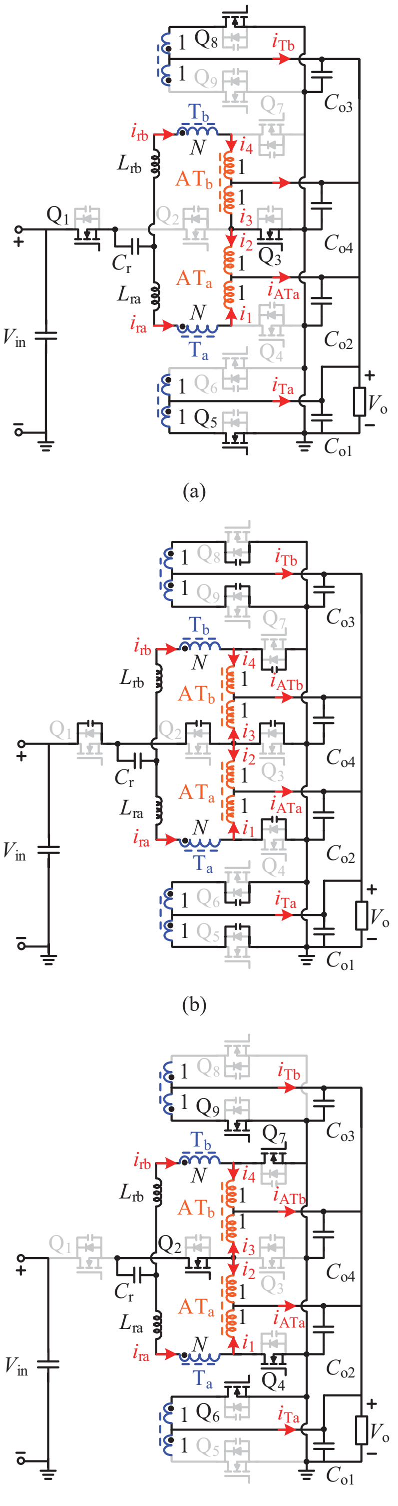

(c)

Fig. 9. Equivalent circuits of each switching mode. (a) Mode I, (b) Mode II and IV, and (c) Mode III.

circuit of each mode is shown in Fig. 9.

Mode I [t_0–t_1] [see Fig. 9(a)]: At t_0, switch Q_1, Q_3, Q_5 and Q_8 are on with zero-voltage switching. The capacitor C_r resonates with the inductor L_{ra}, and L_{rb} to t_1. In this time period, the following relationship will hold if the magnetizing current is ignored:

$$\begin{aligned} i_{ra}(t) &= i_{rb}(t) = i_1(t) = i_2(t) = i_3(t) = i_4(t) \\ &= i_{Ta}(t)/N = i_{Tb}(t)/N \end{aligned} \tag{2}$$

The current flowing through Q_3 is:

$$i_{Q3}(t) = i_2(t) + i_3(t) \tag{3}$$

Meanwhile, the current flowing through Q_5 and Q_8 is:

$$i_{Q5}(t) = i_{Q8}(t) = i_{Ta}(t) = i_{Tb}(t) \tag{4}$$

The voltage applied on Q_2, Q_4, Q_6, Q_7 and Q_9 are:

$$\begin{cases} v_{Q2}(t) = V_{in} \\ v_{Q4}(t) = v_{Q6}(t) = v_{Q7}(t) = v_{Q9}(t) = 2V_o \end{cases} \tag{5}$$

The voltage applied to the winding of the autotransformer is V_o and the voltage at the primary winding of the transformer is NV_o. In this case, there is a voltage relationship:

$$V_{in} = V_{Cr} + NV_o + 2V_o \tag{6}$$

where V_{Cr} is the dc-bias voltage across C_r.

Mode II [t_1–t_2] [see Fig. 9(b)]: At t_1, Q_1, Q_3, Q_5 and Q_8 are off. The operating mode of the converter enters dead time. Within this period, Q_1 drain-source voltage is charged from 0 to V_{in}–$2V_o$. Q_3, Q_5 and Q_8 drain-source voltage are charged from 0 to $2V_o$. Switch Q_2, Q_4, Q_6, Q_7, and Q_9 drain-source voltage are discharge to 0.

Mode III [t_2–t_3] [see Fig. 8(c)]: At t_2, Q_2, Q_4, Q_6, Q_7 and Q_9 are on with zero-voltage switching. C_r resonates with L_r until the t_3. The operating state in this period is similar to Mode I. The following relationship will hold if the magnetizing current is ignored:

$$\begin{aligned} -i_{ra}(t) &= -i_{rb}(t) = i_1(t) = i_2(t) = i_3(t) = i_4(t) \\ &= i_{Ta}(t)/N = i_{Tb}(t)/N. \end{aligned} \tag{7}$$

The current flowing through Q_4 and Q_7 are:

$$i_{Q4}(t) = i_{Q7}(t) = i_1(t) - i_r(t) = i_1(t) + i_{Ta}(t)/N \tag{8}$$

The current flowing through Q_6 and Q_9 are:

$$i_{Q6}(t) = i_{Q9}(t) = i_{Ta}(t) = i_{Tb}(t) \tag{9}$$

The voltage applied on Q_1, Q_3, Q_5 and Q_8 are:

$$\begin{cases} v_{Q1}(t) = V_{in} - 2V_o \\ v_{Q3}(t) = v_{Q5}(t) = v_{Q8}(t) = 2V_o \end{cases} \tag{10}$$

During this period, the voltage relationship in the loop is:

$$V_{Cr} = NV_o + 2V_o \tag{11}$$

where V_{Cr} is also the dc-bias voltage across C_r.

Mode IV [t_3–t_4] [see Fig. 9(b)]: At t_3, Q_2, Q_4, Q_6, Q_7 and Q_9 are off. The circuit enters dead time. Similar to Mode II, in Mode IV, the drain-source voltages of Q_1, Q_3, Q_5 and Q_8

are discharged while the drain-source voltages of Q_2, Q_4, Q_6, Q_7 and Q_9 are charged. During this interval, the circuit will be ready for the soft switching of the active switches at the beginning of the next switching cycle.

Substitute (11) into (6):

$$V_{\text{in}} = 2NV_{\text{o}} + 4V_{\text{o}} \tag{12}$$

The gain G of the circuit can be expressed as:

$$G = \frac{V_{\text{in}}}{V_{\text{o}}} = 2N + 4 \tag{13}$$

According to (13), by configuring the winding turn ratio N of the transformers, different voltage conversion ratios can be realized on the improved non-isolated resonant converter. An 8:1 bus converter can be built if the turn ratio of the two transformers is $N = 2$. Based on the proposed improved non-isolated resonant converter, the magnetic core integration method is adopted for high power density integration design.

III. MAGNETIC CORE INTEGRATION DESIGN OF IMPROVED NON-ISOLATED RESONANT CONVERTER

A. Multi-Core Intergration

As illustrated in Fig. 7, four transformers are used in the improved non-isolated resonant converter. The power density and efficiency of the converter affected dramatically by the footprint, volume, and losses of the cores. However, the volt-second product of the four transformers is the same, because the outputs of these transformers are in parallel, and the secondary windings of these transformers are all one turn. Thus, the four transformers can be realized with one integrated core.

Suppose each transformer uses an EI core, the magnetic core of T_a and AT_a are lined up, as illustrated in Fig. 10(a), where i_{LmT} is the direction of transformer magnetizing current and i_{LmAT} is the direction of autotransformer magnetizing current. The flux magnitude of each core side-leg is equal, but the direction of flux in the adjacent side-leg is reversed. If the adjacent side-legs are merged, the total flux in the merged core-leg will be zero. So, one of the side-leg of EI core can be removed. The two cores are integrated into a four-leg core, as shown in Fig. 10(b). The magnetic core of T_b and AT_b can also be integrated into the four-leg core. The working modes of T_a and T_b are consistent, and that of AT_a and AT_b are consistent. The magnetic flux changes in T_a and T_b magnetic core are consistent, and the magnetic flux changes in magnetic core of AT_a and AT_b are also consistent. Further, the T_a and T_b share one magnetic leg, and the AT_a and AT_b share one magnetic leg, as shown in Fig. 10(c), where i_{LmTa} and i_{LmTb} are the direction of transformer magnetizing current and the direction of autotransformer magnetizing current are i_{LmATa} and i_{LmATb}. The final integrated core has only four magnetic legs, and the footprint, volume and loss of the integrated transformer are reduced.

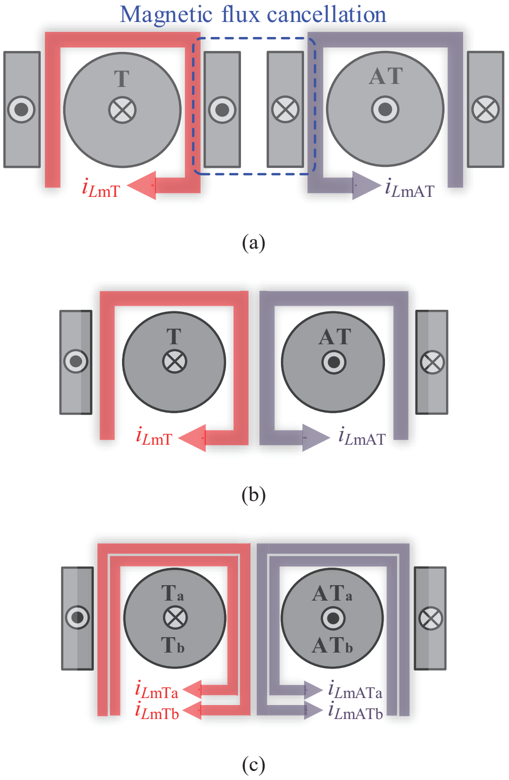

(a)

(b)

(c)

Fig. 10. Multi-core integration. (a) Two EI cores. (b) Integrated core with merged core-legs. (c) Final integrated core.

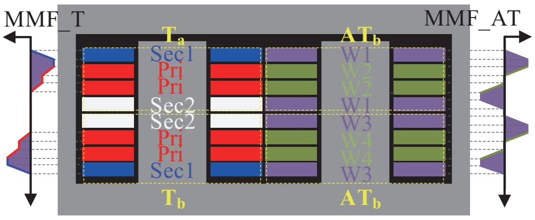

Fig. 11. Winding laminated structure.

B. Winding Stack Design

The transformer turns ratio N is 2:1 for the converter shown in Fig. 7. For a single transformer, it requires at least 4 layers of printed circuit board (PCB) winding. Based on the core integrated structure shown in Fig. 10(c), the converter shown in Fig. 7 requires at least 8 layers of PCB winding. The winding layout of T_a, T_b, AT_a and AT_b is shown in Fig. 11. For T_a and T_b, the primary and the secondary windings are all staggered. The AT_a winding, W1 and W2, and AT_b winding, W3 and W4, also adopt the staggered winding structure. Therefore, the current sharing of parallel winding can be realized. With the PCB winding arrangement shown in Fig. 11, the magnetomotive force (MMF) of the transformer is minimized to reduce the ac resistance and conduction losses of these windings.

C. Integrated Transformer Structure Size Optimization

Fig. 12 shows the schematic diagram of the integrated magnetic core. The core material is DMR53.

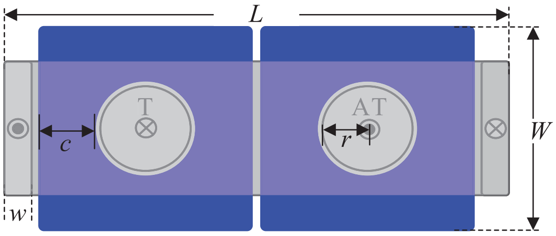

Fig. 12. Transformer dimension diagram.

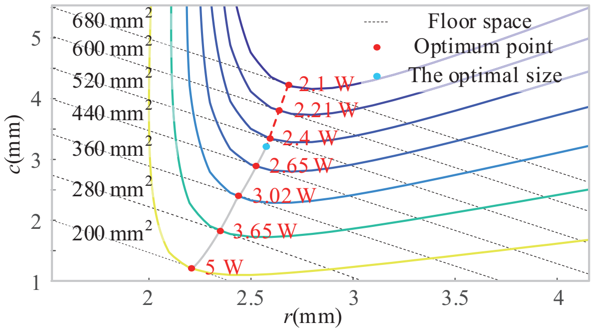

Fig. 13. Transformer optimization curve.

The volume of the magnetic core can be expressed as $V(c, r, w)$, where the width of the winding is c, the radius of the middle core leg is r, the width of the side core leg is w, and the thickness of the top cover is h, where $h = w$. Further, in order to improve the utilization rate of space, the thickness of the top cover is consistent with the height of the devices on the PCB surface. The volume of the magnetic core can be simplified as $V(c, r)$.

The loss of integrated transformer can be divided into core loss and winding loss. The core loss can be used to calculate by the Steinmetz formula:

$$\begin{cases} P_{\text{core}}(c,r) = P_{\text{v}} V(c,r) \\ P_{\text{v}} = C_{\text{m}} f^{x} B^{y} \end{cases} \tag{14}$$

P_{v} is the loss of the magnetic core under different magnetic densities, and the Steinmetz parameters C_{m}, x, y are provided by the material datasheet. The winding loss can be calculated by the AC loss model proposed in [20]. According to the loss model, the total loss of the transformer under different sizes can be calculated and the curve of the relationship between loss and size can be drawn, as shown in Fig. 13.

The dashed lines in Fig. 13 represent the same footprint with different r and c. The solid curve represents the equal loss of the integrated magnetic component for different r and c. The red point where the dashed line is tangent to the solid curve is the smallest total loss point. According to size and loss limit, the blue point in Fig. 13 is the optimal size.

IV. EXPERIMENTAL RESULTS AND ANALYSIS

TABLE I

KEY PARAMETERS OF THE PROTOTYPE

Parameter	Values	Parameter	Values
V_{in}	40–60 V	V_{o}	5–7.5 V
Q_1, Q_2	EPC2218	Q_3–Q_9	IQE006NE2LM5
Gate Dri.	LMG1205	Core	DMR53
I_{o}	80 A	f_{s}	1 MHz

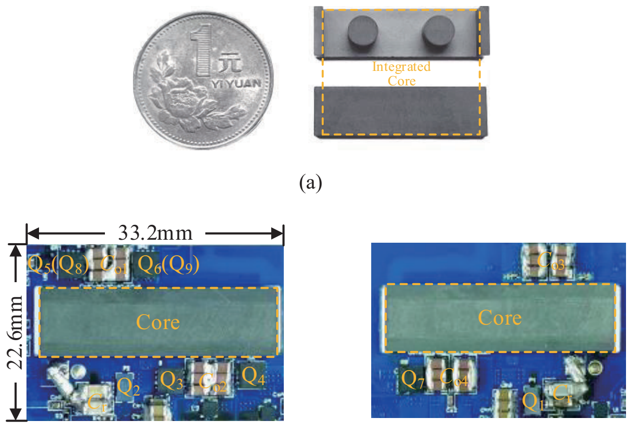

(a)

(b)

(c)

Fig. 14. Experimental prototype. (a) Integrated core. (b) Above prototype. (c) Below prototype.

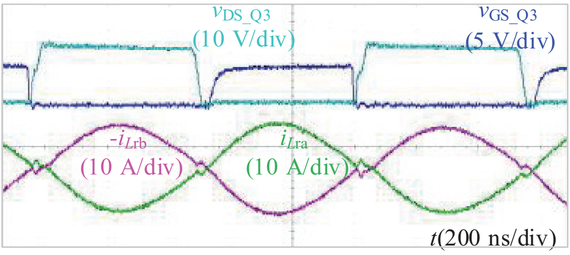

Fig. 15. Resonant current waveform.

Based on the analysis and design, an 8:1 conversion ratio improved non-isolated resonant converter prototype is built. The key parameters of the prototype are shown in Table I. Due to the converter has good soft-switching characteristics, the switching frequency of the converter can reach 1MHz by adopting GaN devices for Q_1 and Q_2. The high switching frequency helps to reduce the volume of transformer and further improve the power density of the converter. In addition, based on the integrated structure of the magnetic core and the equal current flowing through the second synchronous rectifier, Q_5 and Q_8 can be a common switch, Q_6 and Q_9 can also be a common switch. Fig. 14 shows the integrated core and the prototype. The size of the prototype is 33.2 mm (length) × 22.6 mm (width) × 6.8 mm (height). The power density of the prototype is up to 1.734 kW/in^3.

As shown in Fig. 15, the currents flowing through the resonant inductor L_{ra} and L_{rb} are exactly equal. The steady-state waveforms of the drain-source voltage of the switches with

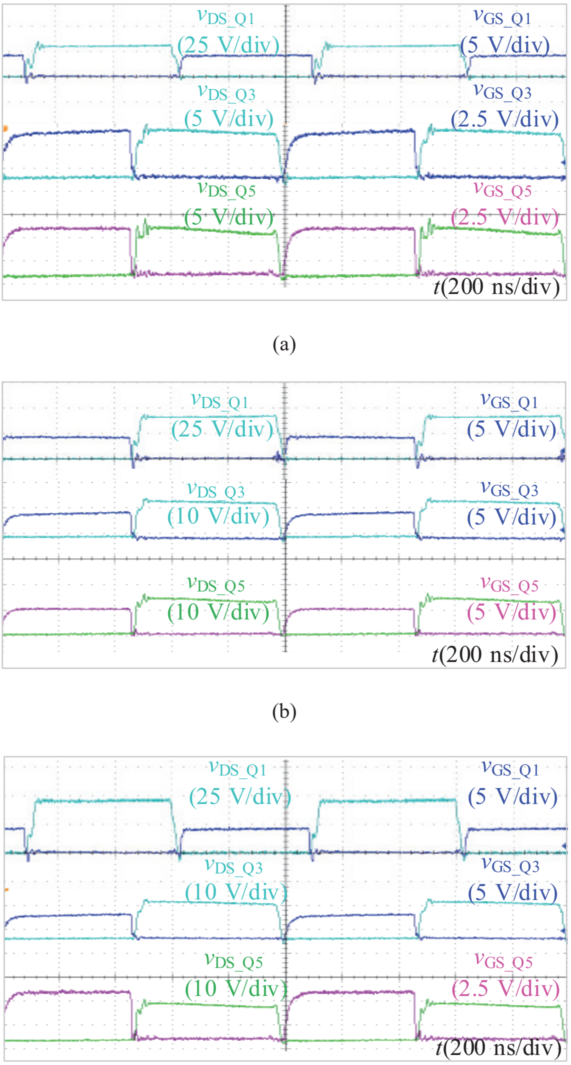

(a)

(b)

(c)

Fig. 16. Drain-source voltage waveform. (a) V_{in} = 40 V. (b) V_{in} = 54 V. (c) V_{in} = 60 V.

40, 54 and 60 V input voltage are shown in Fig. 16, where it is seen that zero-voltage-switching is achieved for all switches.

The efficiency curves of the prototype are shown in Fig. 17. The peak efficiency with 54 V input voltage reaches 98.2%. The full load efficiency is 96%. Considering the gate driver loss is 1 W, the peak efficiency is 97.55%, and the full load efficiency is 95.85%. The thermal distribution of the experimental prototype with full load and forced air cooling is shown in Fig. 18. The fan speed is about 500 linear feet per minute (LFM), and the room temperature is about 25 °C.

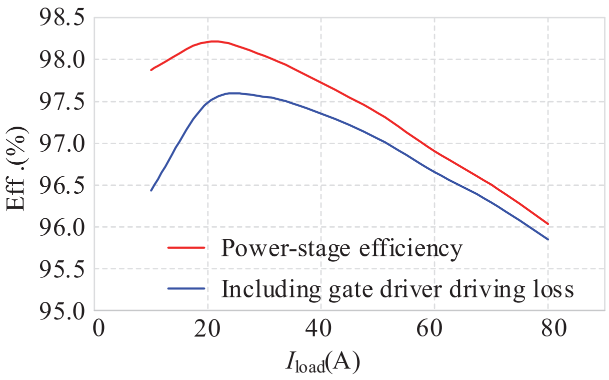

Fig. 17. Efficiency curves.

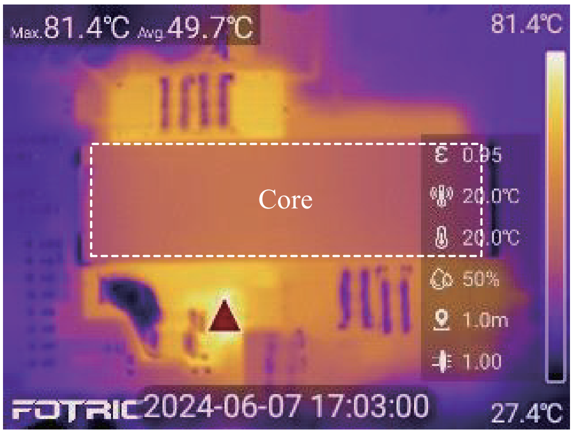

Fig. 18. Thermal distribution with full load and forced air colling.

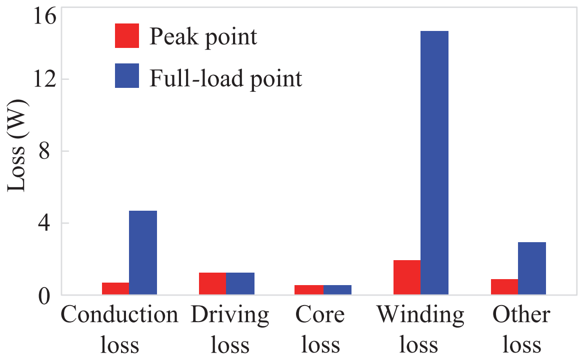

Fig. 19. The loss composition of the converter.

The loss of the prototype mainly includes conduction loss, driving loss, core loss, winding loss, and other loss. The other loss mainly includes termination losses, connection losses between devices and so on. The loss composition at the peak efficiency and full load efficiency with 54 V input voltage is shown in Fig. 19. The gate driver driving loss and core loss are invariable losses which will not going to change with the changed load. The conduction loss, winding loss and other loss are related to the changed load.

The comparative analysis of the proposed solution with the state-of-art works has been provided in Table II. This work achieves high power density and high peak load efficiency. Because of the few PCB winding layers, the full load efficiency is not the highest one. The major contribution of this work is that the dc-bias issue of the high-frequency transformer in the half-bridge non-isolated resonant converter is revealed and solved. The cost of the improved topology is more switches and sub-transformers, which will complex the

TABLE II
PERFORMANCE COMPARISON OF THIS WORK WITH STATE-OF-THE-ART SOLUTIONS

State of art	Turns ratio	Output voltage (V)/Current(A)	Efficiency/%		Number of layers of PCB	Power density of transformer/(kW·in^{-3})
			Peak	Full-load		
[6]	8:1	6.75 /134	98	97.5	12	1.2
[14]	8:1	6 /134	98.1	96.6	14	0.24
[18]	8:1	6.75 /111	98.55	97.3	18	0.74
[19]	8:1	6 /75	97.85	96.6	12	1.18
This work	8:1	6.75 /80	98.2	96	8	1.734

topology and increase the cost. So, a challenge induced by the proposed topology is the design and implementation of multiple transformers. Therefore, more efforts are needed to the integration, structure and parameters optimization of the high frequency transformer.

V. CONCLUSION

An improved non-isolated half-bridge resonant converter is investigated in this paper. Matrix transformer/autotransformer is employed to achieve a symmetrical topology structure. The matrix transformers with paralleled outputs make the presented converter suitable for high current applications. High step-down voltage conversion ratio with reduced transformer turns-ratio has been achieved. Integrated magnetic structure with PCB windings is designed and implemented to achieve high power density. An experimental prototype with an input voltage of 40 V to 60 V, rated output power of 540 W, peak efficiency of 98.2%, and power density of 1.734 kW/in^3 is built and tested to verify the feasibility of the proposed converter. The proposed converter is a good candidate for the bus converter of 48 V data center power supply systems.

REFERENCES

[1] J. Nicola, "How to stop data centres from gobbling up the world's electricity," in *Nature*, vol. 561, no. 7722, pp. 163–166, 2018.

[2] J. Liang, L. Wang, M. Fu, J. Liang, and H. Wang, "Overview of voltage regulator modules in 48 V bus-based data center power systems," in *CPSS Transactions on Power Electronics and Applications*, vol. 7, no. 3, pp. 283–299, Sept. 2022.

[3] J. Baek, Y. Elasser, K. Radhakrishnan, H. Gan, J. P. Douglas, H. K. Krishnam, X. Li, S. Jiang, C. R. Sullivan, and M. Chen, "Vertical stacked LEGO-PoL CPU voltage regulator," in *IEEE Transactions on Power Electronics*, vol. 37, no. 6, pp. 6305–6322, Jun. 2022.

[4] S. Jiang , S. Saggini, C. Nan, X. Li, C. Chung, and M. Yazdani, "Switched tank converters," in *IEEE Transactions on Power Electronics*, vol. 34, no. 6, pp. 5048–5062, 2019.

[5] C. Y. Cai, M. H. Ahmed, Q. Li, and F. C. Lee, "Optimal design of megahertz LLC converter for 48-V bus converter application," in *IEEE Journal of Emerging and Selected Topics in Power Electronics*, vol. 8, no. 1, pp. 495–505, Mar. 2020.

[6] A M. H. Ahmed, F. C. Lee, and Q. Li, "Two-stage 48-V VRM with intermediate bus voltage optimization for data centers," in *IEEE Journal of Emerging and Selected Topics in Power Electronics*, vol. 9, no. 1, pp. 702–715, Feb. 2021.

[7] Y. Chen, H. Cheng, D. M. Giuliano, and M. Chen, "A 93.7% efficient 400A 48V-1V merged-two-stage hybrid switched-capacitor converter with 24V virtual intermediate bus and coupled inductors," in *Proceedings of 2021 IEEE Applied Power Electronics Conference and Exposition (APEC)*, Phoenix, AZ, USA, 2021, pp. 1308–1315.

[8] Z. Tian, Y. Guan, W. Wang, and D. Xu, "Research on high efficiency and high density 48 V-5 V multi-resonant switched capacitor converter," in *CPSS Transactions on Power Electronics and Applications*, vol. 7, no. 3, pp. 229–238, Sept. 2022.

[9] Y. Zhu, T. Ge, N. M. Ellis, L. Horowitz, and R. C. N. Pilawa-Podgurski, "A 500-A/48-to-1-V switching bus converter: A hybrid switched-capacitor voltage regulator with 94.7% peak efficiency and 464-W/in^3 power density," in *Proceedings of 2023 IEEE Applied Power Electronics Conference and Exposition (APEC)*, Orlando, FL, USA, 2023, pp. 1989–1996,

[10] Z. Ye, Y. Lei, and R. C. N. Pilawa-Podgurski, "The cascaded resonant converter: A hybrid switched-capacitor topology with high power density and efficiency," in *IEEE Transactions on Power Electronics*, vol. 35, no. 5, pp. 4946–4958, May 2020.

[11] T. Ge, Z. Ye, and R. Pilawa-Podgurski, "A 48-to-12 V cascaded multi-resonant switched capacitor converter with 4700 W/in^3 power density and 98.9% efficiency," in *Proceedings of 2021 IEEE Energy Conversion Congress and Exposition (ECCE)*, 2021, pp. 1959–1965.

[12] Z. Ye, R. A. Abramson, Y. L. Syu, and R. C. N. Pilawa-Podgurski, "MLB-PoL: A high performance hybrid converter for direct 48 V to point-of-load applications," in *Proceedings of 2020 IEEE 21st Workshop on Control and Modeling for Power Electronics (COMPEL)*, Aalborg, Denmark, 2020, pp. 1–8.

[13] C. Rainer, R. Rizzolatti, and D. Varajao, "High density cascaded ZVS switched capacitor converter for 48-V data-center application," in *Proceedings of PCIM Europe digital days 2020; International Exhibition and Conference for Power Electronics, Intelligent Motion, Renewable Energy and Energy Management*, Germany, 2020, pp. 1–8.

[14] C. Wang, M. Li, Z. Ouyang, Z. Zhang, G. Zsurzsan, and M. A. E. Andersen, "High step-down single-stage DC-DC converter with improved planar matrix transformer for high-current data center application," in *Proceedings of 2022 IEEE Applied Power Electronics Conference and Exposition (APEC)*, Houston, TX, USA, 2022, pp. 709–715.

[15] M. H. Ahmed, A. Nabih, F. C. Lee, and Q. Li, "Low-loss integrated inductor and transformer structure and application in regulated LLC converter for 48-V bus converter," in *IEEE Journal of Emerging and Selected Topics in Power Electronics*, vol. 8, no. 1, pp. 589–600, Mar. 2020.

[16] D. Huang, X. Wu, and F. C. Lee, "Novel non-isolated LLC resonant converters," in *Proceedings of 2012 Twenty-Seventh Annual IEEE Applied Power Electronics Conference and Exposition (APEC)*, Orlando, FL, USA, 2012, pp. 1373–1380.

[17] M. Qiu, M. Wei, X. Liu, H. Meng, and D. Cao, "A family of novel switch capacitor based integrated Matrix autotransformer LLC converter for data center application," in *Proceedings of 2023 IEEE Green Technologies Conference (GreenTech)*, Denver, CO, USA, 2023, pp. 118–122.

[18] R. Rizzolatti, C. Rainer, S. Saggini, and M. Ursino, "High density hybrid switched capacitor converter for data-center application," in *Proceedings*

of 2021 IEEE Applied Power Electronics Conference and Exposition (APEC), Phoenix, AZ, USA, 2021, pp. 1288–1293.

[19] R. Rizzolatti, C. Rainer, S. Saggini, and M. Ursino, "Ultra-low profile hybrid switched capacitor converter with Matrix multi-tapped autostransformer," in *Proceedings of 2021 IEEE Applied Power Electronics Conference and Exposition (APEC)*, Phoenix, AZ, USA, 2021, pp. 869–874.

[20] P. L. Dowell, "Effects of eddy currents in transformer windings," in *Proceedings of the Institution of Electrical Engineers*, vol. 113, no. 8, pp. 1387–1394, 1966.

Zewei Li was born in Sichuan Province, China, in 2001. He received the B.S. degree in electrical engineering from Nanjing University of Aeronautics and Astronautics (NUAA), Nanjing, China, in 2023, where he is currently working toward the M.S. degree in electrical engineering. His main research interests include DC/DC converters and magnetic integration.

Yuanchi Zhang was born in Zhejiang Province, China, in 2002. He received the B.S. degree in electrical engineering from Nanjing University of Aeronautics and Astronautics (NUAA), Nanjing, China, in 2024. His main research interests include high frequency magnetic technology for power electronics.

Yu Zhang was born in Hubei Province, China, in 1998. He received the B.S. and M.S. degrees in electrical engineering from Nanjing University of Aeronautics and Astronautics (NUAA), Nanjing, China, in 2021 and 2024, respectively. His main research interests include DC/DC converters and magnetic integration.

Yujie Cheng was born in Chengji Village, Shangqiu City, in 1987. He received the B.S. degree in measuring and controlling technology and instrument from Xi'an Jiaotong University in Xi'an, in 2010, and the M.S. degree in power electronics from Xi'an Jiaotong University in Xi'an, in 2013.

Since 2013, he has been working in Nanjng Electronic Devices Institute for about 10 years. He was a senior engineer in 2019. He is the author of 8 articles and 2 inventions. His research interests include the design of LLC resonant converter and applications of GaN devices. He received Science and Technology Progress Award of China Electronics Technology Group Corporation in 2022. Now he is pursuing the Ph.D. at Nanjing University of Aeronautics and Astronautics (NUAA).

Yan Xing received the B.S. and M.S. degrees in automation and electrical engineering from Tsinghua University, Beijing, China, in 1985 and 1988, respectively, and the Ph.D. degree in electrical engineering from Nanjing University of Aeronautics and Astronautics (NUAA), Nanjing, China, in 2000.

Since 1988, she has been with the Faculty of Electrical Engineering, NUAA, and is currently a Professor with the College of Automation Engineering, NUAA. She has authored more than 200 technical papers published in journals and conference proceedings and has also published three books. Her research interests include topology and control for dc-dc and dc-ac converters.

Dr. Xing is an Associate Editor of the *IEEE Transactions On Power Electronics*. She is a member of the Committee on Renewable Energy Systems of the IEEE Industrial Electronics Society.

Hongfei Wu received his B.S. and Ph.D. degrees in electrical engineering and power electronics and power drives from Nanjing University of Aeronautics and Astronautics (NUAA), Nanjing, China, in 2008 and 2013, respectively.

Since 2013, he has been with the Faculty of Electrical Engineering, NUAA, and is currently a Professor with the College of Automation Engineering, NUAA. He has authored and co-authored more than 280 peer-reviewed papers published in journals and conference proceedings. He is the holder of more than 40 Patents. His research interests are high-performance power converters, wide-band-gap device applications, and magnetic integration.

Dr. Wu was the recipient of the Best Associate Editor of *Journal of Power Electronics* (2018), the Outstanding Reviewer of *IEEE Transactions on Power Electronics* (2013, 2022), the Changkong Scholar Award, and the Young Scholar Innovation Award of NUAA (2017). He serves as an Associate Editor of the *IEEE Journal of Emerging and Selected Topics in Power Electronics*, *Journal of Power Electronics, Chinese Journal of Electrical Engineering*, and *Journal of Power Supply*.